Microwave stray radiation losses in vacuum windows

J.W. Oosterbeek [a,*], M. Stern [a], H. Braune [a], K. Ewert [a], M. Hirsch [a], F. Hollmann [a], H.P. Laqua [a],
S. Marsen [a], A. Meier [b], D. Moseev [a], F. Noke [a], A. Reintrog [a], T. Stange [a], R.C. Wolf [a],
the W7-X team

[a] *Max–Planck-Institut für Plasmaphysik, Teilinstitut Greifswald, Wendelsteinstraße 1, 17491 Greifswald, Germany*
[b] *Karlsruhe Institute of Technology, Institute for Applied Materials, Hermann-von-Helmholtz-Platz 1, 76344 Eggenstein-Leopoldshafen, Germany*

ARTICLE INFO

ABSTRACT

Vacuum windows are required in magnetically confined fusion experiments to provide possibilities to observe the plasma in a wide range of electromagnetic wavelengths. The window disk consists of a dielectric, e.g. Fused Silica (SiO_2), Sapphire or Chemically Vapourised Diamond (CVD). As electromagnetic waves pass through the disk, a fraction of the beam power is dissipated resulting in a temperature increase of the disk. In Electron Cyclotron Waves (ECW) heated plasmas the dissipation in the window disk can be very high. The computation of dielectric losses for a collimated beam with known incidence angle, polarisation and loss tangent (measure for the intrinsic dielectric loss) is well established. However, the dielectric losses in diagnostic windows mostly result from *microwave stray radiation*, which results from a modest, but inevitable, fraction of non-absorbed ECW. This fraction diffuses in the vessel by many reflections into rays with random k-vector and with random polarisation. In this work the thermal load on the window disk by microwave stray radiation is assessed. The load by a collimated beam is studied as a function of incidence angle and polarisation allowing to average over a distribution of incident rays. An experiment was commissioned measuring the loss tangent of a number of commercially available SiO_2 disks at low power in an open resonator, and subsequently measuring the dielectric heating of these disks at high power stray radiation using the facility 'MISTRAL' at Wendelstein-7X. The experimental results are compared to modelling and it is demonstrated that, in the parameter range considered, single-pass fractional absorption may be applied while taking a safety margin that arises from the minima and maxima due to multiple reflections.

1. Introduction

Thermo-nuclear fusion experiments such as W7-X and ITER use high power microwaves for plasma heating and control. At W7-X the Electron Cyclotron Resonance Heating (ECRH) system has presently 7.5 MW of installed power at 140 GHz, with upgrades in work to bring it up to 20 MW. Microwave power not absorbed by the plasma will diffuse into microwave stray radiation that fills the entire vacuum vessel. This results in a surface power density ($[Wm^{-2}]$) which may be locally analysed using coupled cavities [1,2]. Stray radiation causes thermal loads on in-vessel components. Ohmic heating of the vessel interior is in general no problem as plasma loads are much higher but dielectric heating in ceramics, such as the disks in vacuum windows, must be looked at individually. In this work we report on measurement and modelling of dielectric heating in vacuum windows by stray radiation with the aim to obtain a scaling with the loss tangent of the window disk.

2. Stray radiation response of vacuum window

Plane wave electromagnetic wave propagation in a dielectric slab is well understood [3–6]. Building on this work a model is used to compute the stray radiation response of a dielectric slab as function frequency, permittivity, loss tangent, incidence angle, polarisation and thickness. Wave propagation in dielectric slab is reviewed in this section, limited to the extent that the model can be understood and further developed. In this work fractional power coefficients of reflection (R), transmission (T) and absorption (A) as a percentage are used, i.e. given an input power P_0, reflected power P_r and transmitted power P_t the fractions are: $R = 100(P_r/P_0)$, $T = 100(P_t/P_0)$ and $A = 100(P_a/P_0)$.

The model uses ray tracing to find R, T and A for a plane wave with arbitrary angle of incidence and polarisation. Stray radiation is described as a collection of rays with random k-vector and polarisation, incident on all components as a flux. The stray radiation response is

---

Table 1
Calculation example to judge the scope of approximated A_{SP} (Eq. (2)). A_γ is the non-approximated result by taking the real part of complex γ (for γ see the Appendix) and using exponential decay $e^{-2\alpha z}$ opposed to expanding the exponent. It is concluded that for low loss windows with typical disk thickness the approximation is safe. In doubt, verification and correction is straight forward.

ε_r' [-]	tan δ (x10 $^{-4}$)	d [mm]	A_{SP} [%]	Aγ [%]
3.8	3	6	1.4	1.4
3.8	10	12	6.6	6.9
9.3	5	12	5.2	5.4

Fig. 1. Dielectric Slab, single-pass.

found by averaging R, T and A over a large number of isotropic rays (explanation in Section 2.4). In the summation single sided exposure is used, as is generally the case for vacuum windows. All data is at 140 GHz.

2.1. Single-pass, normal incidence

The window disk is modelled as a dielectric slab shown Fig. 1. A plane wave $E(z,t) = E_0 \left(e^{j\omega t - \gamma z} \right)$ at normal incidence is first considered, i.e. $\theta_i = 0$. The direction of propagation is z, the angular frequency $\omega = 2\pi f$ and the propagation constant $\gamma = \alpha + j\beta$, with α the attenuation constant and β the phase constant. Without losses $\alpha = 0$ and $\beta = 2\pi/\lambda$, with λ the wavelength inside the dielectric which is the vacuum wavelength divided by the refractive index n. In this work the relative permittivity is used throughout with the relationship $n = \sqrt{\epsilon_r'}$. The prime expresses the real part of the relative complex permittivity, which is defined as $\epsilon_r = \epsilon_r' - j\epsilon_r''$. In this expression ϵ_r''/ϵ_r' is the loss tangent, or tanδ, which is the ratio of the conduction current density over the displacement current density. The impedance left of the slab is that of free space denoted by $\eta_1 = \sqrt{\mu_0/\epsilon_0}$ and the impedance of the dielectric is $\eta_2 = \sqrt{\mu_0/\epsilon_0\epsilon_r}$. The impedance mismatch on the interface $\eta_1 \to \eta_2$ gives rise to a reflected fraction of power R_{SP}, where subscript $_{SP}$ stands for Single Pass. The fraction that is transmitted over the interface continues through the slab and is reduced by fractional loss A_{SP}. As the wave exits the slab, per definition of the single-pass case, no internal reflection is accounted for. Note that the absorbed fraction is relative to the incident power and not to the power transmitted into the slab. The reflected electric field at the interface is ΓE_0, with Γ obtained from the boundary conditions on the interface [4]:

$$\Gamma = \frac{\eta_2 - \eta_1}{\eta_1 + \eta_2} = \frac{1 - \sqrt{\epsilon_r'}}{1 + \sqrt{\epsilon_r'}}, \tag{1}$$

where ϵ_r' is taken opposed to ϵ_r as tanδ $\ll$ 1. The reflected fraction of power R_{SP} is the square of Γ as both fractions are in the same medium. Validation of the approximation for the reflected fraction: for tanδ > 0.1 onwards a difference of 0.1% in R using ϵ_r' opposed to ϵ_r, negligible for this work. The single-pass loss is found by substitution of the plane wave in the Maxwell Equations. For tanδ $\ll$ 1 one finds [5]: $\alpha = \pi\sqrt{\epsilon_r'}\tan\delta/\lambda_0$. The electric field in the dielectric attenuates as $e^{-\alpha z}$ and the power as $e^{-2\alpha z}$. As $\alpha z \ll 1$ the exponent can be expanded and the power is attenuated by a factor $2\alpha z$ after the single pass:

$$A_{SP} = \frac{2\pi}{\lambda_0}\sqrt{\epsilon_r'} \cdot \tan\delta \cdot d, \tag{2}$$

with d the window thickness. The transmitted fraction $T_{SP} = 1 - R_{SP} - A_{SP}$. As an example for a SiO$_2$ window with $d = 6$ mm, $\epsilon_r' = 3.8$, tanδ $= 0.001$: $R_{SP} \approx 10\%$, $A_{SP} \approx 3\%$, $T_{SP} \approx 87\%$.

For the single-pass absorption result in Eq. (2) two approximations were made using the condition tanδ $\ll$ 1: (i) extracting α from the propagation constant γ (see the Appendix), and (ii) expanding the exponent ($e^{-2\alpha z}$). To quantify the scope of the approximations see Table 1.
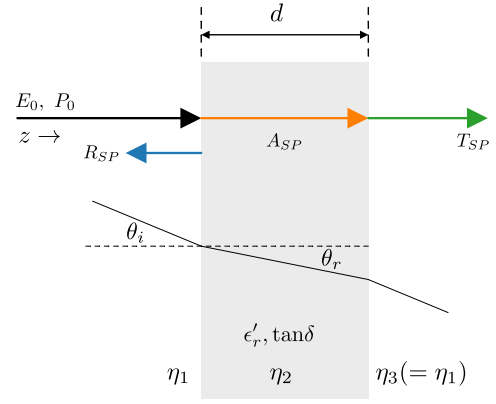
2.2. Multiple reflections, normal incidence

In the multiple reflections case, reflection on each interface is considered, see Fig. 2. By doing so, internal reflections in the slab are accounted for and the fractions are now written with subscript $_{MP}$ for Multi-Pass. To obtain R_{MP}, T_{MP} and A_{MP}, one must sum the phase and the amplitude of the individual – in principle infinite – components. However, the components form series that converge and analytical expressions are available [3,6–8]. The summation of the phases leads to interference fringes as function of the wavelength and the thickness of the slab as illustrated in Fig. 3. Destructive interference in reflection is referred to as a resonant window. In such case the initial reflected fraction is in counter phase with the sum of all subsequent round-trip internal reflections. The resonant thickness is $d = n\frac{1}{2}\lambda_0/\sqrt{\epsilon_r'}$ with n a positive integer. For constructive interference a maximum in reflection is obtained, i.e. an anti-resonant window, for which $d = m\frac{1}{4}\lambda_0/\sqrt{\epsilon_r'}$ with m odd. To assess the absorbed fraction in the multiple reflections case, a zoom on the losses is given in Fig. 4. The absorption peaks at the resonant thickness as maximal power enters the slab in such case. In the resonant case the peaked absorption may be approximated by A_{Res} [6]:

$$A_{Res} \approx \frac{\pi}{\lambda_0}\tan\delta \left(1 + \epsilon_r'\right) d. \tag{3}$$

Plotting this result as a function of d, i.e. also for non-resonant windows, an over-estimate is made as seen by the curve A$_{RES}$ in Fig. 4.

The repetitive pattern in the components for reflection and transmission can also be programmed and summed over an arbitrary number of internal reflections [3]. Following this methodology, the model developed in this work is shown in the Appendix. In the model the round-trip phase delay is accounted for by $\phi = 2\beta d$. The total reflected and total transmitted electric field is obtained by summing all components, i.e. for R the components rc$_0$, rc$_1$, rc$_2$,...,rc$_n$, and for T the components tc$_0$, tc$_1$, tc$_2$,...,tc$_n$. The fractions of reflected and transmitted power, both taken outside the slab, are found by taking the complex conjugate of the summed electric fields. Already after 2 internal reflections, i.e. rc and tc with indices $_{0,1,2}$, a perfect match by eye with Fig. 3 is obtained.

2.3. Oblique incidence

Oblique incidence occurs for $0° < \theta_i < 90°$. In such case the location of the minima and maxima is modified by the different optical path. The amplitudes of the minima and maxima are modified as the electric field reflection and transmission coefficients now depend on incidence angle and polarisation as expressed by the Fresnel equations.
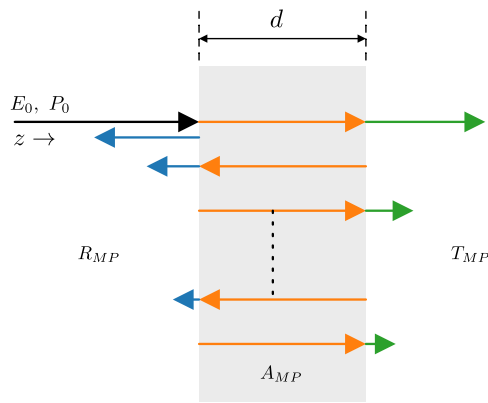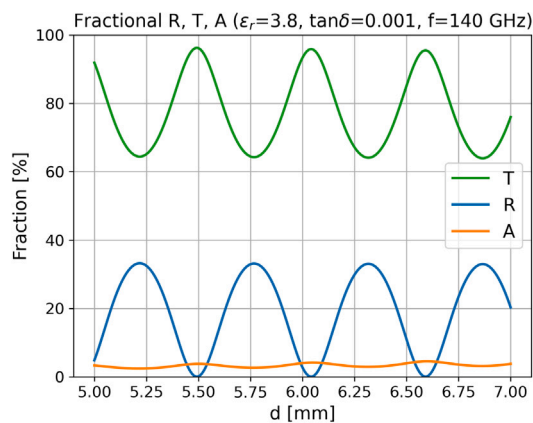
Fig. 2. Dielectric Slab, multi-pass.

Fig. 5. Addition of wavefronts under oblique incidence, (a) principle and (b) zoom. The phase delay between equal phase fronts is the difference in phase between A_1 and A_2.

Fig. 3. Interference due to internal reflections for a plane wave at normal incidence on a typical SiO$_2$ disk. The disk is said to be resonant at 5.49 mm, 6.05 mm and 6.59 mm. The plot was made using analytical expressions for reflection and transmission in a dielectric slab [3], including the complex permittivity, and setting $A = 100\% - T - R$.
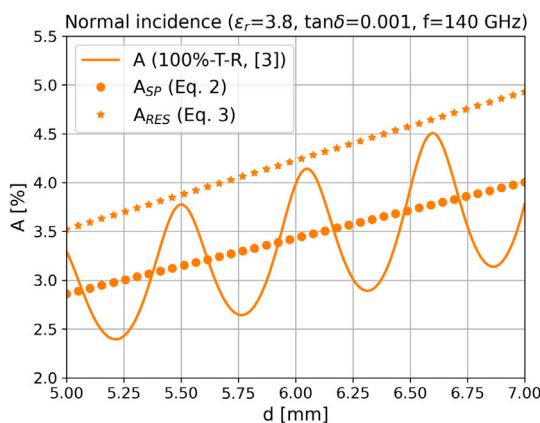

Fig. 4. Zoom on the absorbed fraction in Fig. 3. For comparison the single-pass case (Eq. (2)) and the expression for a resonant window (Eq. (3)) are shown as well.
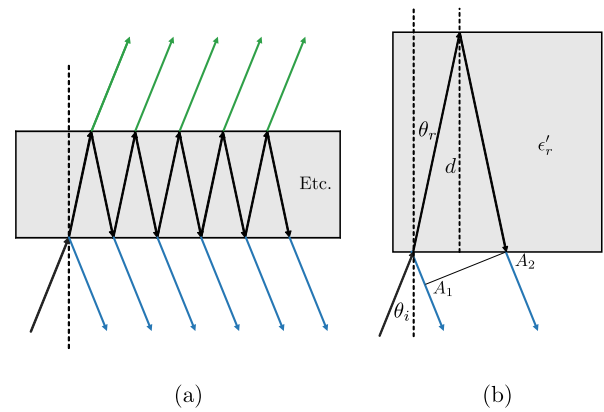
The change in location of the minima and maxima is accounted for by changing the round trip phase delay from $2\beta d$ to $2\beta d \cos\theta_r$, which is found by evaluating the phase delay between A_1 and A_2, see Fig. 5 [7]. A practical issue is that, at very large incidence angles, the ratio of slab diameter over slab thickness must be large enough that still sufficient internal reflections can add up as the rays eventually 'walk off' the slab. At the maximum angle of incidence of $\theta_i = 90°$ and a permittivity of $\epsilon'_r = 3.8$ the refracted angle is $\theta_r = 31°$. Considering a typical window thickness of $d = 6$ mm, the displacement along the slab is 7.2 mm, i.e. of the order of the window thickness. For typical vacuum windows tens of internal reflections are still possible.

The modification in amplitude is given by the Fresnel coefficients [3]:

$$\Gamma_\perp = \frac{\eta_2 \cos\theta_i - \eta_1 \cos\theta_r}{\eta_2 \cos\theta_i + \eta_1 \cos\theta_r} \tag{4a}$$

$$\Gamma_\parallel = \frac{-\eta_1 \cos\theta_i + \eta_2 \cos\theta_r}{\eta_1 \cos\theta_i + \eta_2 \cos\theta_r} \tag{4b}$$

$$t_\perp = \frac{2\eta_2 \cos\theta_i}{\eta_2 \cos\theta_i + \eta_1 \cos\theta_r} \tag{5a}$$

$$t_\parallel = \frac{2\eta_2 \cos\theta_i}{\eta_1 \cos\theta_i + \eta_2 \cos\theta_r} \tag{5b}$$

To illustrate the dependence of reflected power on incidence angle, Fig. 6 shows squared coefficients $\Gamma_{b\perp}$ and $\Gamma_{b\parallel}$ as function of incidence angle for a SiO$_2$ surface. At small incidence angles the expression for R at normal incidence holds (Eq. (1) squared), then the two polarisations diverge: $R_\perp$ increases while $R_\parallel$ decreases and vanishes at the Brewster angle. Continuing to very large incidence angles both $R_\perp$ and $R_\parallel$ reach full reflection. The curves may be interpreted as reflections off a slab with very large thickness, or with very high losses, leading to negligible internal reflections. Fig. 7 shows the reflected fractions in case of a slab of SiO$_2$, i.e. a volume such as a typical vacuum window. Now there is the combined effect of the Fresnel coefficients and multiple internal reflections. Given the particular window thickness and permittivity, a minimum occurs close to the Brewster angle. A thicker window results in more minima, and it has been verified that when using a very large loss tangent indeed Fig. 6 is returned.

To compute the absorbed fraction under oblique incidence the path length through the dielectric must be taken: $d' = d / \cos\theta_r$, as the path for evaluating the phase fronts results in an under-estimate.

At large incidence angles, $\theta_i > 85°$, the reflection coefficient approaches unity. Any small fraction that is still coupled into the disk
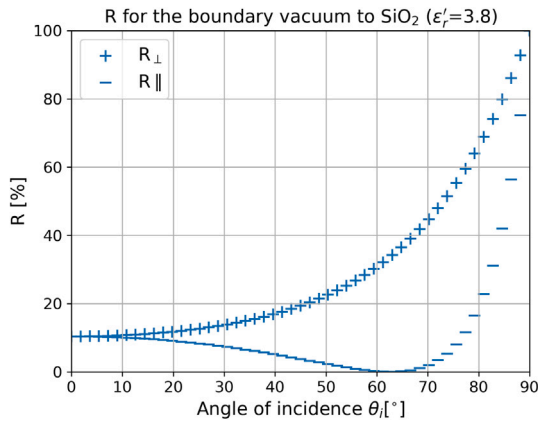
Fig. 6. Squared Fresnel coefficients as function of incidence angle for reflection off the initial interface only (no internal reflections). The minimum at $R_\parallel$ at 63° is the Brewster angle.

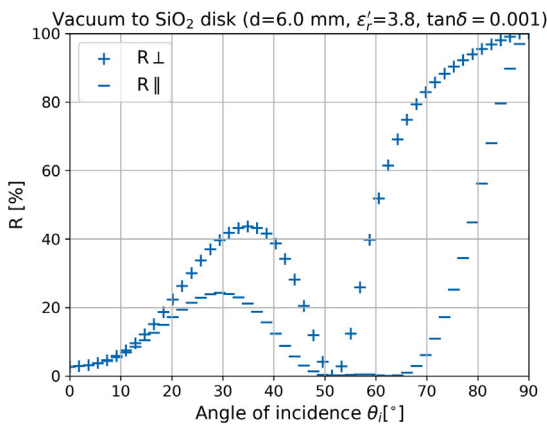

Fig. 7. $R_\perp$ and $R_\parallel$ as function of θ_i, now including internal reflections. At this particular combination of thickness, permittivity and incidence angle, an interference minimum appears in the vicinity of the Brewster angle. Note that at d = 6.0 mm (and $\epsilon'_r = 3.8$) the window is close to resonant explaining the low reflection at normal incidence.

makes many passes inside the disk: it can be seen as 'trapped'. In such case considerable internal reflections must be taken into account as attenuation now determines how many internal reflections it takes before the amplitude of the electric field becomes negligible, not the fraction coupled out of the disk at each interface. In the model 25 internal reflections are used by default.

2.4. Disk exposed to stray radiation

The microwave stray radiation inside the vacuum vessel is taken to be isotropic with both polarisations equally present. To express the vacuum window response to isotropic stray radiation, the fractions R, T and A are now written with subscript $_{ISO}$. The fractions R_{ISO}, T_{ISO} and A_{ISO} are obtained by illuminating one side of the window with isotropic rays. An isotropic ray is a 3D unity vector on the window surface such as the green ray illustrated in the cartoon in Fig. 8. The red line is a unity vector along the z-axis and the two grey lines represent the x- and y-axis. The incidence angle θ_i is the inverse cosine of the dot-product between the red vector and the green vector. The dots on the
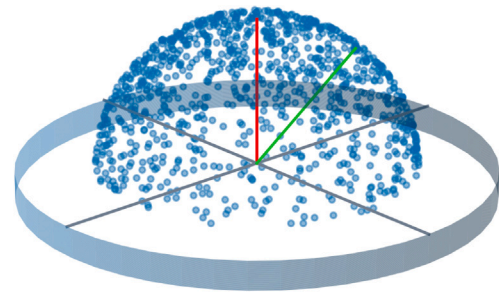

Fig. 8. Random points on a sphere used to obtain isotropic rays incident on the window surface. Each dot represents an incident ray, 1000 are shown but in simulations typically 5000 are taken. Rays with small incidence angles are less pronounced as rays with large incidence angles.
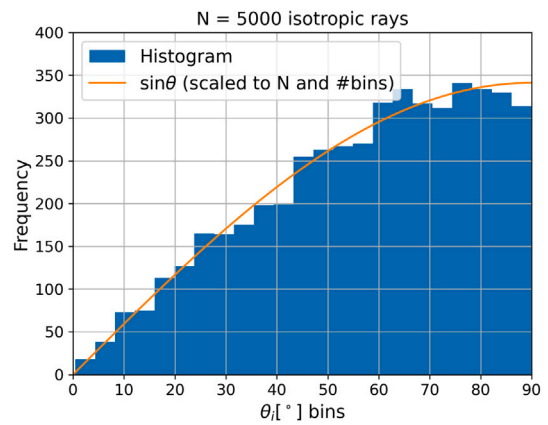

Fig. 9. Histogram with distribution of incident rays.

unity half sphere represent incident rays going through x, y, z = 0, 0, 0. They are obtained by drawing numbers from a normal distribution and normalising these to unity vectors, resulting in equally spaced points on the sphere surface [9]. These then represent isotropic rays such as used to describe stray radiation [2]. The isotropic rays per unit surface are constant but a circulation around the top of the half sphere is clearly shorter as a circulation around the bottom which means large incidence angle are more pronounced as small incidence angles. The histogram in Fig. 9 confirms the sinusoidal weighting of the rays with incidence angle.

For each ray the fractions R(θ_i) and T(θ_i) are computed for either polarisation. Processing all rays result in 4 quantities as function of incidence angle: $R_\perp(\theta_i)$, $T_\perp(\theta_i)$, $R_\parallel(\theta_i)$, $T_\parallel(\theta_i)$. The absorbed fractions follow from $A_\perp(\theta_i) = 100\% - R_\perp(\theta_i) - T_\perp(\theta_i)$ and $A_\parallel(\theta_i) = 100\% - R_\parallel(\theta_i) - T_\parallel(\theta_i)$. To arrive at the compound values R_{ISO}, T_{ISO} and A_{ISO}, the averages of the fractions ($R_\perp(\theta_i)$, $T_\perp(\theta_i)$, $R_\parallel(\theta_i)$, $T_\parallel(\theta_i)$) are taken by summing the response for each ray and dividing these sums by the number of rays, then as the final step averaging over both polarisations. The process is illustrated in Fig. 10.

Opposed to summing isotropic rays one can also use a weighted average to sum the response of all incidence angles. The weight in such case is the sine of the incidence angle. It was verified that this gives the same results.
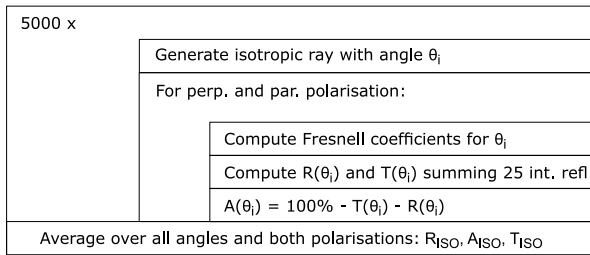
Fig. 10. Computation of R_{ISO}, T_{ISO} and A_{ISO} for stray radiation exposure for fixed thickness.

Fig. 11. Window disk mounted in MISTRAL port geometry and terminated with caloric load. In the cone a pyrometer may be mounted to monitor the window temperature.

3. Experiment

The aim of this work is to find the vacuum window thermal load caused by microwave stray radiation. The absorbed fraction of power A is required as function of the dielectric properties. The power deposited in the disk is – at low temperature and short time scales – proportional to the window heating rate $\Delta T/\Delta t$ [K/s]. One side of the window is exposed to microwave stray radiation while the other side is terminated with a microwave load. The window temperature is monitored at the load side. Given a relatively thin disk and a homogeneous absorption profile, this temperature is a good measure of the deposited energy. Using a simple caloric expression, A is obtained from the heating rate. To interpret the measurements and to validate the model, the reflection fraction R is helpful and is obtained by an insertion loss measurement.

3.1. Samples and loss tangent data

The experimental data is used to verify the model and enables to collect dielectric data around 140 GHz. Quartz, SiO_2, sapphire, ZnSe or CVD Diamond are all candidate materials for the work, but different grades of a SiO_2 were selected given availability and actual use at W-7X. Additionally, reference permittivity and loss tangent data at 140 GHz by Heidinger [10,11] is available. Contacts with suppliers resulted in a collection of samples from which the dielectric properties were measured in open resonators [12,13]. All samples are 5.9 mm thick and have a diameter ranging from 93.3 mm to 94.5 mm. The open resonator laboratory experiments were carried out at the Karlsruhe Institute of Technology (KIT). The samples and the dielectric data are shown in Table 2. The permittivity of the samples was measured at 90 GHz while the loss tangent data is at 142 GHz or 143 GHz due to subtleties in extracting the loss tangent from the resonator measurements. In the modelling and high power measurements 140 GHz is used as this is the MISTRAL gyrotron frequency. The table is combined with the absorbed and reflected fractions using (i) single-pass, (ii) the model and (iii) the high power exposure measurements described next. For the Corning® sample no dielectric data is available as it was added after the tests at KIT.

3.2. High power stray radiation response

3.2.1. MISTRAL

At W7-X a high power stray radiation exposure facility MISTRAL [14–16] is in operation. It is a microwave resonator vessel with diameter 1.5 m and length 2.2 m in which a gyrotron beam is launched. The beam is by means of a launching mirror reflected towards the vessel wall such that it makes a trajectory around the circumsphere while, due to a small tilt angle of the launcher, it also propagates along the vessel. As the beam reaches the far end of the vessel it changes direction and
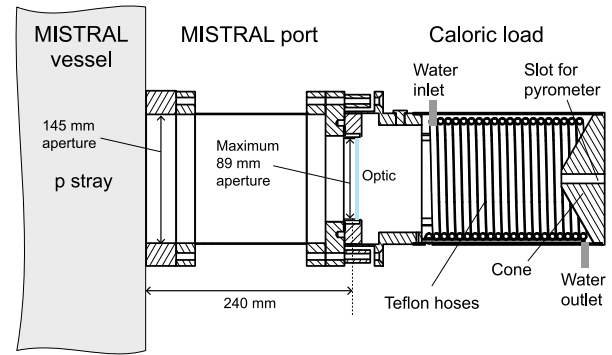
travels back again to the launch side over a similar trajectory, and so forth. On the trajectory the beam reflects many times off the wall, on the way scattering a fraction of power on each reflection, resulting in a stray radiation field along the central axis of the vessel. The gyrotron power is up to 200 kW but is modulated on–off such that at maximum $P_{in} = 10$ kW time averaged power is injected (duty cycle 1:20 in such case). The resulting surface power density in the MISTRAL follows from a power balance consideration [17]. The source term is the injected power and the sink terms are the vessel interior and apertures. In the most basic case the power balance is $p = P_{in}/[(100 - R_w)S_w]$, with p the surface power density [W/m²], R_w the wall reflectivity [%] and S_w the surface of the vessel wall. The aluminum MISTRAL vessel has a very high reflectivity resulting a high surface power density inside the vessel. At the 10 kW time averaged input power, the surface stray radiation power density, during the MISTRAL campaigns described here, was measured as $p = (55 \pm 5)$ kWm^{-2}. Normal operation conditions are under vacuum with no limit to the exposure time. Operation without vacuum is also possible but limited to 2 min to reduce the risk of arcing at elevated temperatures. Items can be placed inside the vessel or mounted onto the vessel.

3.2.2. Caloric load

For the measurement of the stray radiation response the window disk was mounted in a port on the vessel. This is a realistic geometry and it also allows measurement of the power by terminating the port with a caloric load. Fig. 11 shows a sketch of the arrangement. The load was purposely developed for the window exposure experiments with the following requirements: (i) operating at a nominal load of 300 W CW (DN100 window with 89 mm aperture and 50 kWm^{-2} power density), (ii) a caloric measurement on the cooling water to get the deposited power with a resolution of 5 W, and (iii) reflection coefficient of the load low enough to consider single sided exposure only, set by requiring the load reflection coefficient to be below the caloric measurement accuracy, i.e. to below 1.5%. The load was realised using Teflon hoses with cooling water wound along the inside. At the far end a microwave reflective cone is mounted. A stray radiation flux entering the load is either absorbed by initial passes over the Teflon hoses or reflects off the cone at the far end and then onto the hoses. The flow of the cooling water as well as the temperature difference between inlet and outlet are measured, which gives the absorbed power by a simple caloric consideration. An electrical heater, inserted between the inlet temperature gauge and the water inlet, allows an absolute calibration by measurement of the heater voltage and current.

The stray radiation measurement arrangement was commissioned by (i) verifying the microwave pattern through the port and (ii) making
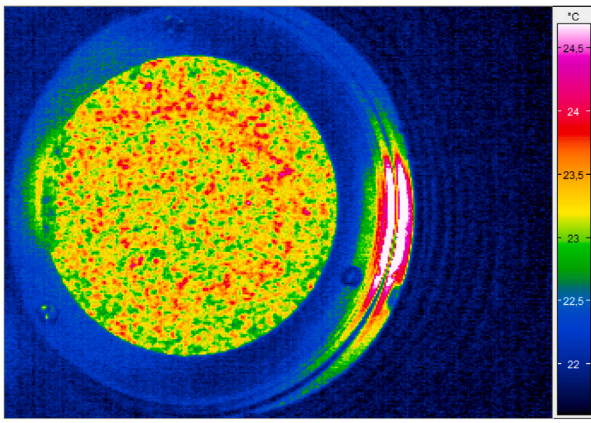
Fig. 12. IR-recording of thermographic paper mounted on a disk mounted in the port. The absorbed stray radiation power scales with the colour-bar. The aperture diameter is 89 mm. The speckles are caused by minima and maxima in the electric field and changed between recordings, indicative of a stray radiation field.
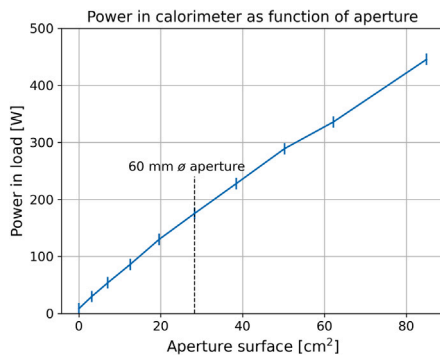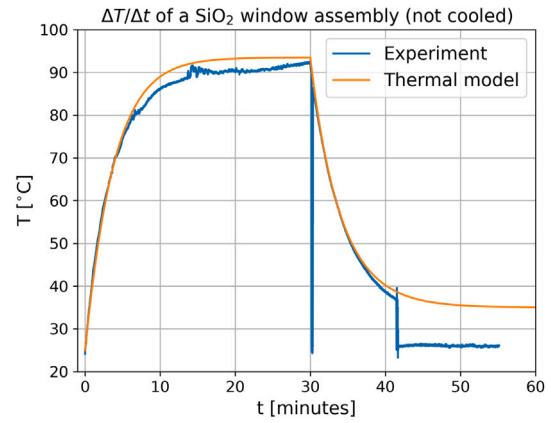

Fig. 14. Stray radiation exposure of an ITER prototype SiO$_2$ window (aperture 60 mm, thickness 6 mm). MISTRAL input power setting 10 kW CW. The temperature was monitored with a pyrometer mounted in the caloric load. The spike at 30 min is caused by briefly replacing the pyrometer by a surface temperature probe for calibration.
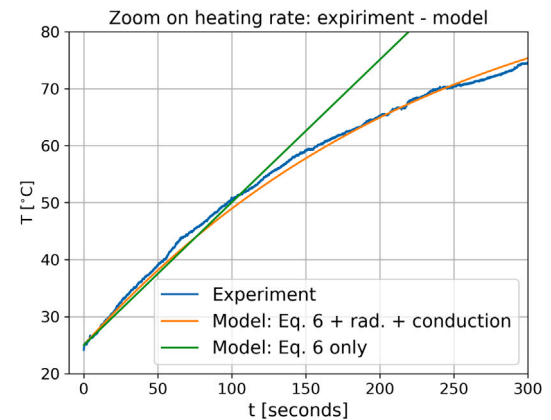

Fig. 13. Aperture scan showing linearity of the load: window insertion loss may be directly inferred from the relative drop of power upon insertion. The small offset on the curve was noted and eliminated during the measurements.

Fig. 15. Heating rate measured and modelled.

a scan of power using different apertures to check the linearity of the caloric load (refer to subsection 'Aperture scaling').

Microwave pattern. The microwave pattern was investigated by replacing the cone with an infra-red camera and by placing microwave absorbing thermographic paper on a disk mounted in the port. The MISTRAL was used at nominal gyrotron power (200 kW) with 20 pulses of 250 μs using a duty cycle 1:5. See Fig. 12.

Aperture scaling. For the aperture scan the disk was removed and replaced with apertures increasing in surface, see Fig. 13. The data point at surface zero is a fully closed aperture, then, left to right, followed by apertures with diameter 20, 30, 40, 50, 60, 70, 80, 89 and 104 mm, the last point in fact with the aperture holder removed. In the experiments the 60 mm aperture was used (surface ≈ 28 cm^2). It is seen that the calorimeter responds linearly to applied input power such that window insertion loss may be directly obtained from the relative drop in power upon inserting a window between the port and the load.

3.2.3. Measurement of heating rate

The temperature increase ΔT of the disk is equated to energy increase ΔE:

$$\Delta T = \frac{\Delta E}{m \cdot c_v} \Leftrightarrow \frac{\Delta T}{\Delta t} = \frac{P_{abs}}{m \cdot c_v}, \tag{6}$$

with m the mass and c_v the specific heat of SiO$_2$. The linear increase of temperature with energy is only valid by neglecting heat transport by radiation and conduction. To assess this, a measurement using a full window assembly is shown in Fig. 14. The plot shows the temperature evolution of a SiO$_2$ window during stray radiation exposure using the 10 kW CW input setting of the MISTRAL. Using a thermal model, following methodology by [18], a fit is shown too in the plot that includes a radiation and a conduction term. To verify that one can neglect radiation and absorption at low temperatures, a zoom during the first minutes is shown in Fig. 15 with the thermal model versus Eq. (6). It is seen that at low temperatures Eq. (6) is good approximation for the heating rate.

The temperature is recorded by the pyrometer with the emissivity calibrated against a surface temperature probe. While the pyrometer is very useful for the overall temperature recording, the surface temperature probe has an absolute calibration and a 0.1 °C accuracy. It is therefore used for the disk temperature measurements by taking the temperature just before exposure and immediately after exposure. The surface probe is show in Fig. 16. The samples were measured with the MISTRAL at atmospheric pressure. As an example the measurement on the Heraeus sample Spectrosil® 2000 is described.
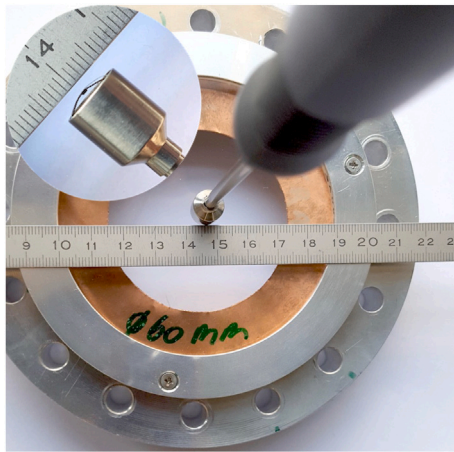
Fig. 16. Measurement of the window temperature by using a surface temperature probe. This method, opposed to using the pyrometer, was found to give an absolutely calibrated temperature measurement with a reproducibility within a degree C. It does require removal of the rear of the water load, but this was facilitated by a clip allowing the measurement to be taken within seconds after exposure. The probe tip has very little mass and is spring loaded for good thermal contact.

With the MISTRAL input power set at 10 kW CW, a 60 s pulse was made. The central window temperature before exposure was 21.9 °C and afterwards 36.5 °C. The heating rate is $\Delta T/\Delta t = (0.24 \pm 0.02)$ K/s. The error derives from an estimate of 1 °C uncertainty in the temperature due to the small delays in measurement before and after exposure as well as from a small gradient (order 1 °C) in temperature between the window centre and the window edge over the 60 s pulse, the gradient limited too by the poor thermal conductivity of SiO_2. The central window temperature was consistently used in the measurements. The absorbed power $P_{abs} = (\Delta T/\Delta t) \cdot m \cdot c_v = (6.4 \pm 0.4)$ W, with $c_v = 715$ J/(kgK) and m = 37 g, found by weighing the sample and scaling it to the exposed aperture surface.

3.2.4. Measurement of insertion loss

Using the 60 mm aperture and no disk, the incident power measured with the calorimeter was (168 ± 5) W. Next the disk was inserted while keeping the 60 mm aperture in place, giving (117 ± 5) W. The insertion loss is therefore $((168 - 117)/168) \times 100 = (30 \pm 5)$ %. The experimental absorbed fraction A_{exp} is $(6.4 \pm 0.4)/(168 \pm 5) = (3.8 \pm 0.4)\% = 3.8\%$ with a 10% relative error. The experimental reflected fraction is the insertion loss minus the absorbed fraction: $R_{exp} = (26 \pm 5)\% = 26\%$ with a 20% relative error.

3.2.5. Measurement table

For each sample it was proceeded as in Sections 3.2.3 and 3.2.4 with the results given in Table 2.

4. Discussion

Comparison between measurement and model shows that for A_{ISO} mostly a slight under-estimate is obtained and for R_{ISO} a rather large over-estimate. Recalling that (i) the reflected fraction goes to unity at large incidence angles, (ii) large incidence angles are more pronounced as small incidence angles, but (iii) that the window is mounted in a port geometry hindering large incidence angles, a hypothesis is that the model gives the large incidence angles too much weight for a measurement in a port geometry. To test this hypothesis A_{ISO} and R_{ISO} are computed as a function of a maximum incidence angle θ_{max}. As an example, limiting the incidence angle to 70° would result in a

Table 2

Measurement and modelling results. Samples by Heraeus: HR, sample by Torr Scientific: TS, sample by Corning®: CN. Note: where the uncertainty is given as a percentage, it is the relative error on the specific entry. Example: a 10% uncertainty on A_{exp} of 1.6% means $A_{exp} = (1.6 \pm 0.16)\%$.

| Thickness: 5.9 mm	Open resonator			Fractions A and R (@140 GHz)					
	f [GHz]	tan δ (x10⁻⁴)	ε_r' @ 90 GHz	A_{SP} [%]	A_{ISO} [%]	A_{EXP} [%]	R_{SP} [%]	R_{ISO} [%]	R_{EXP} [%]
Uncertainty:		±20%	±0.1	±20%		±10%	±5%		±20%
HR: Suprasil® 300	143	4.3	3.80	1.5	1.2	1.6	10	40	26
HR: Spectrosil® 2000	142	12.6	3.83	4.3	3.6	3.8	10	40	26
HR: Suprasil® 313	143	6.6	3.81	2.2	1.9	2.3	10	41	26
HR: Infrasil® 302	143	4.2	3.80	1.4	1.2	1.5	10	40	23
HR: HOQ® 310	143	4.3	3.81	1.5	1.3	1.8	10	40	26
TS: 'Own grade'	142	11.6	3.82	3.9	3.3	3.4	10	40	26
CN: C7980 1D	-	-	-	-	-	3.4	-	-	27
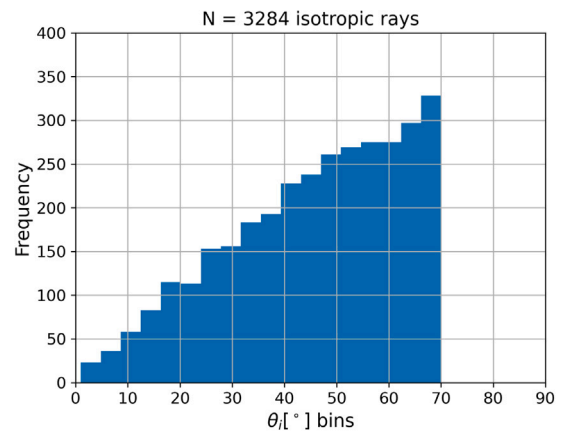
Fig. 17. Histogram with incidence angles reduced to 70°.

distribution as shown in Fig. 17. A_{ISO} and R_{ISO} are computed as a function of maximum incidence angle for the Heraeus Spectrosil® 2000 sample, see Fig. 18 (note the different ordinates for R_{ISO} and A_{ISO}). The absorbed fraction varies as expected inversely with the reflected fraction. When allowing only small incidence angles the reflected fraction is around the single-pass result ($R_{SP} = 10.4\%$) as the window is neither resonant (6.04 mm, n = 11) nor anti-resonant (5.77 mm, m = 21). When allowing all incidence angles the reflection increases, as may be expected from Fig. 6. Recalling that the measured reflected fraction was 26 %, this corresponds to limiting incidence angles to 75°. Limiting the incidence angles to 75° and recomputing A_{ISO} and R_{ISO} for all samples leads to revised Table 3. The modelled reflected fractions are all lower and now very close to the experimental values. Given the lower reflection, the absorbed fractions are slightly higher, resulting in a net improvement too between modelled and experimentally found absorbed fractions.

Cutting off at $\theta_i = 75°$ is a rather crude adjustment but it supports the hypothesis that the weight of extreme incidence angles must be reduced for a window in a port geometry.

The single-pass loss gives periodic under- and over-estimates as is seen in Fig. 4. This is because it does not account for resonances and anti-resonances in the reflected power. The single-pass loss agrees well with stray radiation losses, both measurements and the model, at the thickness of $d = 5.9$ mm. A question that arises is whether the minima and maxima as function of thickness still occur if stray radiation exposure is used. The available samples did not allow to make a scan in thickness but the model can be used to make a first assessment. In Fig. 19 A_{ISO} is shown as a function of disk thickness: for $\theta_{max} = 10°$ as a benchmark, and for $\theta_{max} = 75°$ as for a window in port geometry.
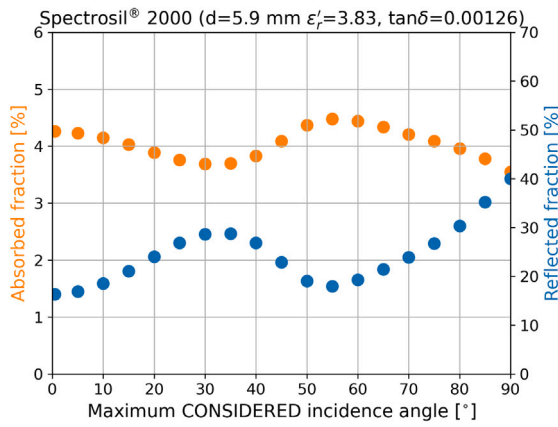
Fig. 18. A_{ISO} and R_{ISO} as function of maximum incidence angle.
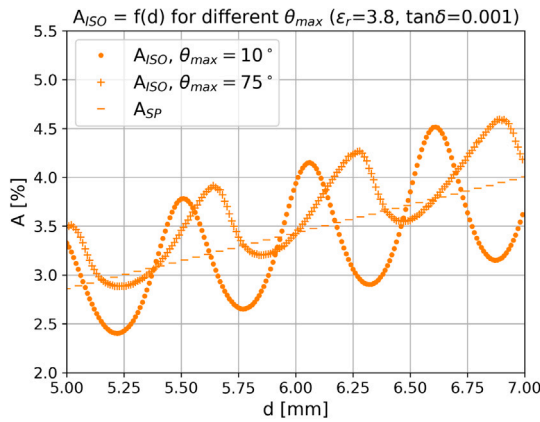

Fig. 19. Stray radiation response as a function of window thickness. As a benchmark normal incidence is modelled by considering isotropic angles up to 10°. The trace considering isotropic angles up to 75° is the stray radiation response. Minima and maxima are predicted to still occur, but with modifications to phase and amplitude.

Table 3
A_{ISO} and R_{ISO} revised for limiting incidence angles to 75°. Note: where the uncertainty is given as a percentage, it is the relative error on the specific entry, see also the example in Table 2.

Thickness: 5.9 mm	Open resonator			Fractions A and R (@140 GHz)					
	f [GHz]	tan δ (x10^{-4})	ε_r' @ 90 GHz	A_{SP} [%]	A_{ISO} [%]	A_{EXP} [%]	R_{SP} [%]	R_{ISO} [%]	R_{EXP} [%]
Uncertainty:		±20%	±0.1	±20%		±10%	±5%		±20%
HR: Suprasil® 300	143	4.3	3.80	1.5	1.4	1.6	10	28	26
HR: Spectrosil® 2000	142	12.6	3.83	4.3	4.1	3.8	10	27	26
HR: Suprasil® 313	143	6.6	3.81	2.2	2.2	2.3	10	27	26
HR: Infrasil® 302	143	4.2	3.80	1.4	1.4	1.5	10	27	23
HR: HOQ® 310	143	4.3	3.81	1.5	1.4	1.8	10	27	26
TS: 'Own grade'	142	11.6	3.82	3.9	3.8	3.4	10	27	26
CN: C7980 1D	-	-	-	-	-	3.4	-	-	27

When incidence angles up to 10° are considered, indeed the result for normal incidence in Fig. 4 is obtained again. Including angles up to 75° shows that minima and maxima still occur, but with modifications in phase and amplitude. It is stressed that these are modelling results, with points at one thickness (d = 5.9 mm) verified.

Overall it can be concluded that for an assessment of absorption in a port geometry the single-pass approximation in Eq. (2) can be taken, using a safety margin arising from the maxima as in predicted Fig. 19. This is Eq. (3) / Eq. (2) = $(1 + \epsilon_r')/2\sqrt{\epsilon_r'} \approx 1.25$ for SiO_2. A further margin could be set for measurement error, but noting that the samples show good agreement between resonator and high power measurements. Should one expect predominantly small incidence angles, an anti-resonant disk is a good choice. But for a broader range of incident angles this advantage may be lost as the modified optical path length ($d \cos\theta_r$) may give rise to resonances at larger incidence angles.

Variation of loss tangent with temperature has not been investigated in this work but it is in the data of Fig. 14. The source term in the heating rate is given by Eq. (6) with $P_{abs} = p A_{ISO} S$. Setting $A_{ISO} = A_{SP}$ and $m = \rho S d$, with ρ the specific density, the source term becomes:

$$\frac{\Delta T}{\Delta t} = p \frac{2\pi \sqrt{\epsilon_r'} \tan\delta}{\lambda_0 \rho c_v}. \tag{7}$$

Sink terms in the model are radiation, scaling with emissivity σ, and a conduction term. Over the $\approx 80\,K$ temperature difference considered only $\sigma, \tan\delta, \epsilon_r'$, and c_v, and possibly the conduction term, may have a relevant temperature coefficient. In the model, however, these terms are not temperature dependent, yet the fit is reasonable. From this data and model, it is concluded that the temperature coefficient of $\tan\delta$ does not appear large. For concise numbers on variation of loss tangent with temperature, a dedicated experiment with samples at elevated temperature is recommended, such as carried out by Heidinger [19].

CRediT authorship contribution statement

J.W. Oosterbeek: Conceptualization, Investigation, Writing – review & editing. **M. Stern:** Methodology, Software, Investigation. **H. Braune:** Investigation. **K. Ewert:** Investigation. **M. Hirsch:** Conceptualization. **F. Hollmann:** Investigation. **H.P. Laqua:** Conceptualization, Methodology. **S. Marsen:** Investigation. **A. Meier:** Investigation, Methodology. **D. Moseev:** Methodology. **F. Noke:** Investigation. **A. Reintrog:** Investigation. **T. Stange:** Investigation, Methodology, Visualization. **R.C. Wolf:** Supervision. **W7-X team:** Resources, Funding acquisition.
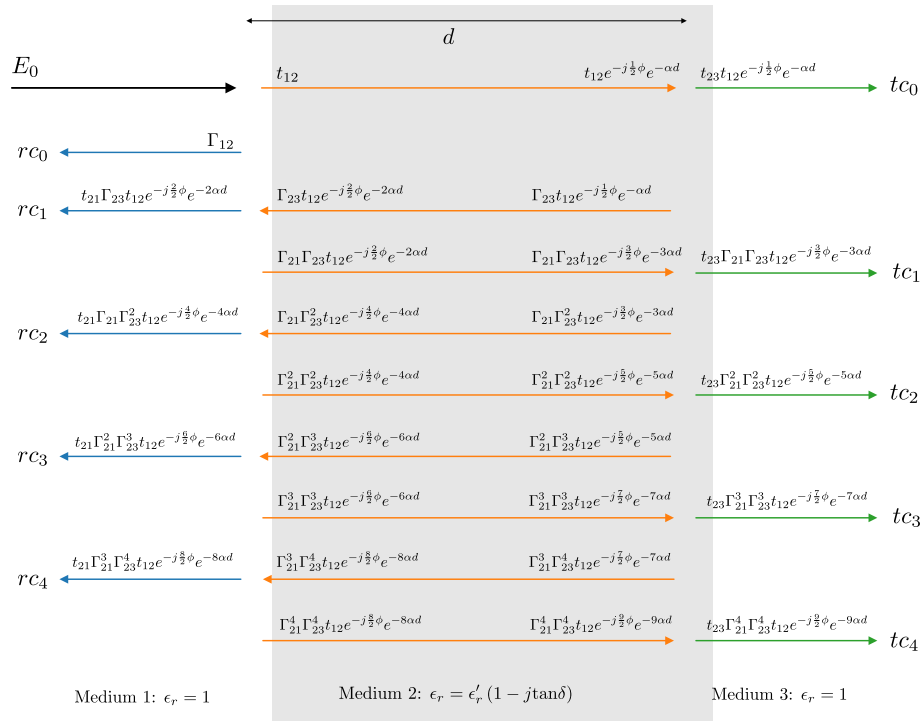
Data availability

Data will be made available on request.

Acknowledgements

Appendix. Model slab with multiple reflections

d

E_0

t_{12} $t_{12}e^{-j\frac{1}{2}\phi}e^{-\alpha d}$ $t_{23}t_{12}e^{-j\frac{1}{2}\phi}e^{-\alpha d}$ tc_0

rc_0 Γ_{12}

rc_1 $t_{21}\Gamma_{23}t_{12}e^{-j\frac{2}{2}\phi}e^{-2\alpha d}$ $\Gamma_{23}t_{12}e^{-j\frac{2}{2}\phi}e^{-2\alpha d}$ $\Gamma_{23}t_{12}e^{-j\frac{1}{2}\phi}e^{-\alpha d}$

$\Gamma_{21}\Gamma_{23}t_{12}e^{-j\frac{2}{2}\phi}e^{-2\alpha d}$ $\Gamma_{21}\Gamma_{23}t_{12}e^{-j\frac{3}{2}\phi}e^{-3\alpha d}$ $t_{23}\Gamma_{21}\Gamma_{23}t_{12}e^{-j\frac{3}{2}\phi}e^{-3\alpha d}$ tc_1

rc_2 $t_{21}\Gamma_{21}\Gamma_{23}^2 t_{12}e^{-j\frac{4}{2}\phi}e^{-4\alpha d}$ $\Gamma_{21}\Gamma_{23}^2 t_{12}e^{-j\frac{4}{2}\phi}e^{-4\alpha d}$ $\Gamma_{21}\Gamma_{23}^2 t_{12}e^{-j\frac{3}{2}\phi}e^{-3\alpha d}$

$\Gamma_{21}^2\Gamma_{23}^2 t_{12}e^{-j\frac{4}{2}\phi}e^{-4\alpha d}$ $\Gamma_{21}^2\Gamma_{23}^2 t_{12}e^{-j\frac{5}{2}\phi}e^{-5\alpha d}$ $t_{23}\Gamma_{21}^2\Gamma_{23}^2 t_{12}e^{-j\frac{5}{2}\phi}e^{-5\alpha d}$ tc_2

rc_3 $t_{21}\Gamma_{21}^2\Gamma_{23}^3 t_{12}e^{-j\frac{6}{2}\phi}e^{-6\alpha d}$ $\Gamma_{21}^2\Gamma_{23}^3 t_{12}e^{-j\frac{6}{2}\phi}e^{-6\alpha d}$ $\Gamma_{21}^2\Gamma_{23}^3 t_{12}e^{-j\frac{5}{2}\phi}e^{-5\alpha d}$

$\Gamma_{21}^3\Gamma_{23}^3 t_{12}e^{-j\frac{6}{2}\phi}e^{-6\alpha d}$ $\Gamma_{21}^3\Gamma_{23}^3 t_{12}e^{-j\frac{7}{2}\phi}e^{-7\alpha d}$ $t_{23}\Gamma_{21}^3\Gamma_{23}^3 t_{12}e^{-j\frac{7}{2}\phi}e^{-7\alpha d}$ tc_3

rc_4 $t_{21}\Gamma_{21}^3\Gamma_{23}^4 t_{12}e^{-j\frac{8}{2}\phi}e^{-8\alpha d}$ $\Gamma_{21}^3\Gamma_{23}^4 t_{12}e^{-j\frac{8}{2}\phi}e^{-8\alpha d}$ $\Gamma_{21}^3\Gamma_{23}^4 t_{12}e^{-j\frac{7}{2}\phi}e^{-7\alpha d}$

$\Gamma_{21}^4\Gamma_{23}^4 t_{12}e^{-j\frac{8}{2}\phi}e^{-8\alpha d}$ $\Gamma_{21}^4\Gamma_{23}^4 t_{12}e^{-j\frac{9}{2}\phi}e^{-9\alpha d}$ $t_{23}\Gamma_{21}^4\Gamma_{23}^4 t_{12}e^{-j\frac{9}{2}\phi}e^{-9\alpha d}$ tc_4

Medium 1: $\epsilon_r = 1$ Medium 2: $\epsilon_r = \epsilon_r'(1-j\tan\delta)$ Medium 3: $\epsilon_r = 1$

$\gamma =$ propagation constant $= j\omega\sqrt{\mu_0\epsilon_0\epsilon_r'}\sqrt{1-j\tan\delta} = \alpha + j\beta.$ [*1)]

$\phi =$ round trip phase delay $= 2\beta d,\quad \eta = \sqrt{\dfrac{\mu_0}{\epsilon_0 \cdot Re(\epsilon_r)}}\ (\mu_r = 1)$

$\Gamma_{12} = \dfrac{\eta_2 - \eta_1}{\eta_1 + \eta_2}, \Gamma_{21} = \dfrac{\eta_1 - \eta_2}{\eta_2 + \eta_1}, \Gamma_{23} = \dfrac{\eta_3 - \eta_2}{\eta_2 + \eta_3}$ $t_{12} = \dfrac{2\eta_2}{\eta_1 + \eta_2}, t_{21} = \dfrac{2\eta_1}{\eta_2 + \eta_1}, t_{23} = \dfrac{2\eta_3}{\eta_2 + \eta_3}$

Reflected field $= E_0(rc_0 + rc_1 + rc_2 + \cdots rc_n) = E_0\Gamma_{sum}$ *Transmitted field* $= E_0(tc_0 + tc_1 + tc_2 + \cdots tc_n) = E_0 t_{sum}$

$\Gamma_{sum} = \Gamma_{12} + t_{12}t_{21}\sum\limits_{n=1}^{n=\infty}\Gamma_{21}^{(n-1)}\Gamma_{23}^{(n)}e^{-jn\phi}e^{-2n\alpha d}$ $t_{sum} = t_{12}t_{23}\sum\limits_{n=0}^{n=\infty}(\Gamma_{21}\Gamma_{23})^n e^{-j(n+1/2)\phi}e^{-(2n+1)\alpha d}$

Fractional reflected power: $R = \Gamma_{sum}\Gamma_{sum}^*$ Fractional transmitted power: $T = t_{sum}t_{sum}^*$

[*1)] For $\tan\delta \ll 1:\ \ \alpha \approx \dfrac{\pi}{\lambda_0}\sqrt{\epsilon_r'}\tan\delta,\ \ \beta \approx \dfrac{2\pi}{\lambda_0}\sqrt{\epsilon_r'}$ (but in the model α=Re(γ) and β=Im(γ) are used).

References

[1] H.P. Laqua, Distribution of the ECRH stray radiation in fusion devices, in: 28th EPS Conference on Contr. Fusion and Plasma Phys. 25A, P3.099, 2001.

[2] D. Moseev, et al., Stray radiation energy fluxes in ITER based on a multiresonator model, Fusion Eng. Des. 172 (2021).

[3] C.A. Balanis, Advanced Engineering Electromagnetics, John Wiley and Sons, 1986.

[4] Samual Y. Liao, Microwave Devices and Circuits, third ed, Prentice Hall, 1990.

[5] S. Ramo, et al., Fields and Waves in Communication Electronics, John Wiley & Sons, Inc., 1994.

[6] H.-U. Nickel, Hochfrequenztechnische Aspekte zur Entwicklung rückwirkungsarmer Ausgangsfenster für Millimeterwellengyrotrons hoher Leistung, Wissenschaftliche Berichte, Forschungszentrum Karlsruhe, FZKA 5513, 1995.

[7] F.A. Jenkins, Fundamentals of Optics, 4-th Edition, McGraw-Hill Book Company, 1981.

[8] J.W. Oosterbeek, et al., Microwave response of ITER vacuum windows, 124, 2017, pp. 442–445.

[9] D.E. Knut, The Art of Computer Programming, Volume 2 / Seminumerical Algorithms, third ed., Addison-Wesley, 1998.

[10] R. Heidinger, Dielectric and mechanical properties of neutron irradiated KU1 and KS-4V glass, Fusion Eng. Des. 66/68 (2003) 843/848.

[11] R. Heidinger, et al., Neutron irradiation studies on window materials for EC wave systems, Fusion Eng. Des. 56/57 (2001) 471/476.

[12] F. Königer, Measurement system for the precise determination of dielectrical properties in the mm-wave range based on hemispherical open resonators, Frequenz 43 (1989).

[13] I. Danilov, R. Heidinger, New approach for open resonator analysis for dielectric measurements at mm-wavelengths, J. European Ceramic Society 23 (2003) 2623–2626.

[14] H.P. Laqua, et al., ECRH heating scenarios and in-vessel components at the Wendelstein7-X stellarator, in: Proceedings of the 14th Joint Workshop on Electron Cyclotron Emission and Electron Cyclotron Resonance Heating, Santorini, Greece, 2006, pp. 9–12.

[15] M. Hirsch, et al., The impact of microwave stray radiation to in-vessel diagnostic components, in: International Conf. on Fusion Reactor Diagnostics, Varenna, 9-13 September 2013, vol. 1612, (39) AIP Conference Proceedings, 2014.

[16] D. Hathiramani, et al., Microwave stray radiation: Measures for steady state diagnostics at wendelstein 7-X, Fusion Eng. Des. 88 (2013) 12321235.

[17] H.J. Hartfuss, et al., Problems with ECRH stray radiation in wendelstein 7-X, in: 30th EPS Conference on Contr. Fusion and Plasma Phys. St. Petersburg, 7-11, vol. 27A, ECA, 2003, O-3.2C.

[18] N. Maassen, Microwave Detector Design for ITER, Technical University of Eindhoven, Internship TU/e Fusion, 2014.

[19] R. Heidinger, et al., MM - Wave characterisation of LOW loss dielectric materials using open resonators, in: ITG-Conference, Display and Vacuum Electronics, 29-30/4/1998, Garmisch Partenkirchen, Germany, 1998, pp. 363–368.